

## LA-UR-14-22914

Approved for public release; distribution is unlimited.

Title: Multiscale X-ray and Proton Imaging of Bismuth-Tin Solidification

Author(s): Gibbs, Paul J.  
Imhoff, Seth D.  
Morris, Christopher  
Merrill, Frank E.  
Wilde, Carl H.  
Mariam, Fesseha G.  
Fezzaa, Kamel  
Lee, Wah-Keat  
Clarke, Amy J.  
Nedrow, Paul

Intended for: JOM

Issued: 2014-07-29 (rev.1)

---

**Disclaimer:**

Los Alamos National Laboratory, an affirmative action/equal opportunity employer, is operated by the Los Alamos National Security, LLC for the National Nuclear Security Administration of the U.S. Department of Energy under contract DE-AC52-06NA25396. By approving this article, the publisher recognizes that the U.S. Government retains nonexclusive, royalty-free license to publish or reproduce the published form of this contribution, or to allow others to do so, for U.S. Government purposes. Los Alamos National Laboratory requests that the publisher identify this article as work performed under the auspices of the U.S. Department of Energy. Los Alamos National Laboratory strongly supports academic freedom and a researcher's right to publish; as an institution, however, the Laboratory does not endorse the viewpoint of a publication or guarantee its technical correctness.

# Multiscale X-ray and Proton Imaging of Bismuth-Tin Solidification

P.J. GIBBS,<sup>1</sup> S.D. IMHOFF,<sup>1</sup> C.L. MORRIS,<sup>1</sup> F.E. MERRILL,<sup>1</sup>  
C.H. WILDE,<sup>1</sup> P. NEDROW,<sup>1</sup> F.G. MARIAM,<sup>1</sup> K. FEZZAA,<sup>2</sup>  
W.-K. LEE,<sup>3</sup> and A.J. CLARKE<sup>1,4</sup>

1.—Los Alamos National Laboratory, P.O. Box 1663 Los Alamos, NM 87545, USA. 2.—Argonne National Laboratory, 9700 South Cass Avenue, Argonne, IL 60439, USA. 3.—Brookhaven National Laboratory, P.O. Box 5000 Upton, NY 11973, USA. 4.—e-mail: aclarke@lanl.gov

The formation of structural patterns during metallic solidification is complex and multiscale in nature, ranging from the nanometer scale, where solid-liquid interface properties are important, to the macroscale, where casting mold filling and intended heat transfer are crucial. X-ray and proton imaging can directly interrogate structure, solute, and fluid flow development in metals from the microscale to the macroscale. X-rays permit high spatiotemporal resolution imaging of microscopic solidification dynamics in thin metal sections. Similarly, high-energy protons permit imaging of mesoscopic and macroscopic solidification dynamics in large sample volumes. In this article, we highlight multiscale x-ray and proton imaging of bismuth-tin alloy solidification to illustrate dynamic measurement of crystal growth rates and solute segregation profiles that can be that can be acquired using these techniques.

## INTRODUCTION

During phase transformations in metal alloys, the relative mobility of solute, interfaces and thermal energy dictate product length scales. These characteristics are particularly relevant in solidification processing, where changes in solute or heat flow can manifest dramatic changes in interface stability. Importantly, the patterning developed at one length scale, such as dendrite arrays, is implicitly tied to larger and smaller length scale phenomena, such as macroscopic heat flow and convection and the liquid-solid interface energy. To accelerate the development, manufacture, and deployment of advanced materials,<sup>1</sup> we must effectively combine theory and modeling with experiments to fundamentally understand microstructural development across multiple length scales.<sup>2,3</sup>

Continuous imaging of metals at the microscopic, mesoscopic, and macroscopic scales during solidification is possible with the use of synchrotron x-ray<sup>4–11</sup> and proton<sup>12</sup> sources. X-rays permit the examination of small metal volumes ( $<1\text{ mm}^3$ ) and thin sections (e.g., 0.1–0.2 mm) at micrometer spatial resolution (e.g.,  $2\text{ }\mu\text{m}$  features).<sup>4–12</sup> The

penetrating power of protons permits imaging of mesoscale and macroscale structure in larger metal volumes (e.g.,  $>10,000\text{ mm}^3$ ) and thicker sections (e.g., 6 mm)<sup>12</sup> at reduced spatial resolution ( $\sim 20\text{--}150\text{ }\mu\text{m}$  features) over larger fields of view than are achievable with x-rays. Direct imaging of metal solidification enables unprecedented understanding of solidification dynamics that will inform model parameterization, development, and verification and will revolutionize solidification technology developments.

In this article, we highlight some examples of multiscale x-ray and proton imaging of structural development in bismuth-tin (Bi-Sn) alloys during solidification. Specifically, bismuth crystal growth dynamics and characteristics are measured and the dynamical development of macrosegregation is presented.

## EXPERIMENTAL METHODS

Synchrotron x-ray imaging was performed at the Sector 32-Insertion Device beamline at Argonne National Laboratory's Advanced Photon Source (APS). A monochromatic 28-keV x-ray beam was

used. X-rays pass through a thin metal foil and impinge upon a scintillator, where they are converted to visible light. A mirror is positioned behind the scintillator and a fast videocamera records the reflected image; the nominal imaging frame rate was 0.46 Hz and the field of view was  $1.4 \times 1.7$  mm. The camera captured images with a demagnified pixel size of  $0.74 \mu\text{m}$ . An 0.1-mm-thick,  $11 \times 30$ -mm metal alloy sample was inserted into a boron nitride crucible; this configuration was inserted into a slotted steel rod with a 5 mm through hole perpendicular to the flat plane of the crucible to accommodate the beam path and permit imaging of the sample foil. The steel rod was heated using two independently controlled water-cooled induction coils centered above and below the sample position; the rod was instrumented with thermocouples to provide temperature monitoring and feedback control. Thermocouples were placed nominally 0.5 mm from the edge of the through hole to measure the thermal gradient across the imaging region. The thermocouples used to control the induction coils were approximately 38 mm away from the center of the imaging through hole. Control of the power to each of the coils allowed for a range of thermal gradients and cooling rates to be imposed on the metal sample. The thermal profile was controlled to solidify the foil from the bottom upward.

Complementary proton imaging of thin and thick metal sections was also performed. Eight hundred MeV multiframe flash proton radiography (pRad), available at Los Alamos National Laboratory's (LANL) Los Alamos Neutron Science Center (LAN-SCE), was invented for dynamic materials studies.<sup>13,14</sup> We have recently pioneered the use of protons to image dynamic phenomena during melting and solidification.<sup>12</sup> A collimator is placed at the Fourier plane of the proton imaging system (a location in the optics where scattering in the object is mapped to radial position) that generates contrast in the proton radiograph by removing protons of a specified angular range. The collimation can be adjusted to optimize the contrast-to-noise ratio for a wide range of object thicknesses, from  $200 \text{ mg cm}^{-2}$  to  $50 \text{ g cm}^{-2}$ . The system has been optimized over the years to resolve  $<1\%$  relative density changes during dynamic experiments.<sup>15</sup> At 800 MeV, proton image resolution is limited by chromatic aberrations of the protons, focused by the magnetic imaging lens, and the resolution of the detector system. A set

of magnifying imaging lenses is placed between the object and the camera system to reduce chromatic aberrations and increase magnification.<sup>16–19</sup> This improves the resolution of the system by both reducing chromatic aberrations and scaling the image size to the experimental region of interest. A summary of the imaging characteristics for the various pRad lenses and x-ray configurations is provided in Table I.

Graphite crucibles with a thinned window area and an internal pocket to hold a metal alloy section were used for dynamic proton imaging experiments. Each crucible was instrumented with thermocouples to provide temperature monitoring and feedback control. The crucible ends were heated using independently controlled induction heaters. The power to each induction coil was controlled, allowing for the desired thermal gradient and cooling rates to be imposed on a metal section. Solidification progressed from the bottom of the section upward in these experiments. Static proton images (without a crucible) were acquired for the 0.1-mm-thick Bi-30 at.% Sn alloy foil imaged with x-rays.

All the transmission radiographs were postprocessed to maximize local contrast of microstructural features of interest and to normalize the grayscale to a consistent reference. Image analysis was performed using ImageJ software (National Institutes of Health, Bethesda, MD, USA).<sup>20</sup> To remove artifacts in the x-ray images resulting from local variations in brightness due to variation in the beam intensity and sample thickness, the total image sequence was divided by the blurred average of a series of images where the sample was fully liquid. For the proton radiographs, the images of the samples were divided by representative images of only the beam to normalize the brightness across the image to account for variations in the beam intensity with position. All of the measurements reported in this study were made on background subtracted images and represent the average of at least three replicate measurements.

## RESULTS AND DISCUSSION

Near-eutectic Sn-Bi alloys are promising potential replacements for lead-containing solder alloys. However, the tendency of bismuth to form faceted crystals during solidification may result in detrimental mechanical behavior.<sup>21</sup> Bismuth can

**Table I. Proton and x-ray imaging characteristics**

Imaging configuration	Spatial resolution ( $\mu\text{m}$ )	Field of view (mm)	Sample size (mm)
pRad identity	150	$120 \times 120$	$40 \times 35 \times 3$
pRad $\times 3$	65	$44 \times 44$	$25 \times 50 \times 6.5$
pRad $\times 7$	25	$17 \times 17$	$4.5 \times 10 \times 0.5$
X-rays at APS 32-ID-C	2	$1.4 \times 1.7$	$10 \times 35 \times 0.2$

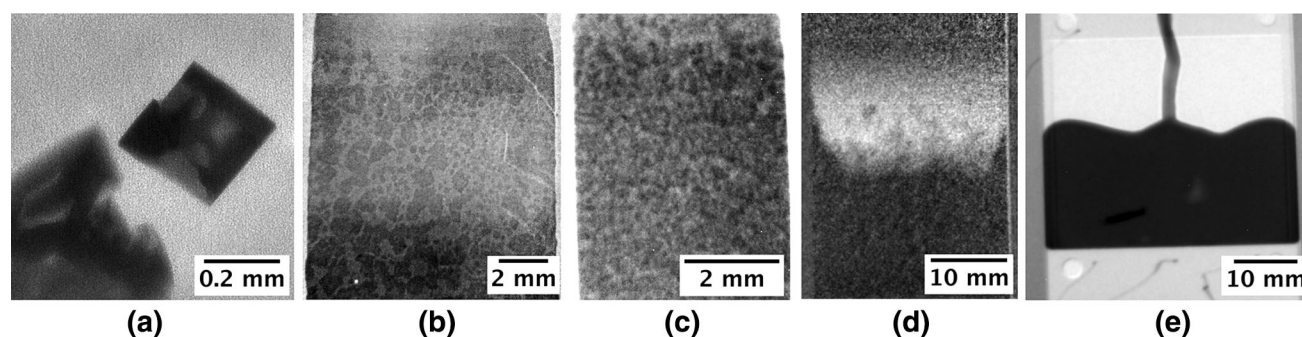


Fig. 1. Example images of multiscale structural development in Bi-30 at.% Sn alloys during directional solidification of (a) a 0.1-mm-thick foil imaged using 28 keV coherent x-rays and proton imaging of (b) the 0.1-mm-thick foil in (a) using the  $\times 7$  magnifier, (c) directional solidification of an 0.5-mm-thick section using the  $\times 7$  magnifier, (d) directional solidification of a 6.5-mm-thick section using the  $\times 3$  configuration, and (e) casting mold filling of a 3-mm-thick plate using the identity lens (Bi-70 at.% Sn alloy). Darker regions correspond to higher density.

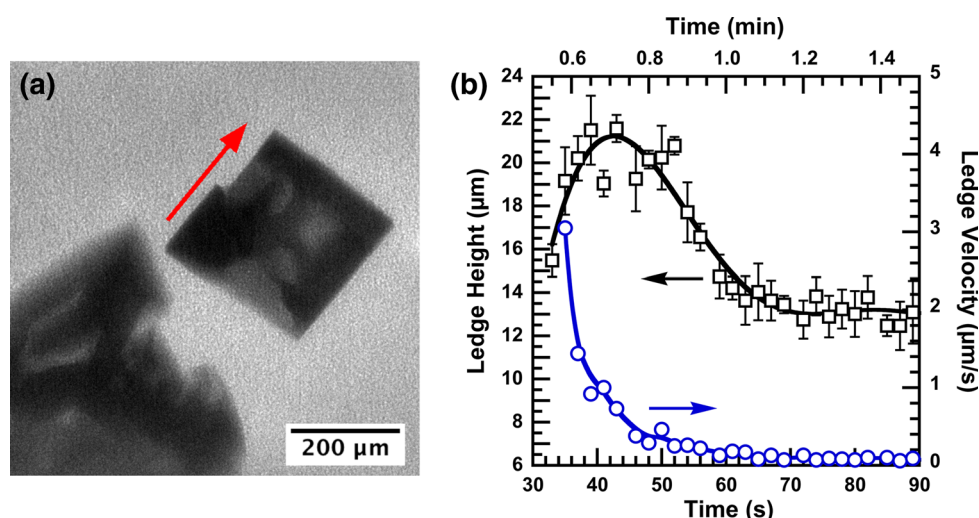


Fig. 2. (a) X-ray image of primary bismuth crystal ledge growth in 0.1-mm-thick foil of a Bi-30 at.% Sn alloy solidified in a constant gradient of  $10^{\circ}\text{C cm}^{-1}$  at a cooling rate of  $20^{\circ}\text{C min}^{-1}$  and (b) the measured ledge height (left axis, squares) and growth velocity (right axis, circles). Times are indexed to the first frame showing the growth of the isolated crystal in (a). The arrow in (a) indicates the growth direction of the step-like ledge on the crystal. The uncertainty limits in (b) represent the standard deviation of three measurements; the uncertainty in the velocity measurements is typically smaller than the plotted symbols. The lines in (b) are intended as a visual guide of the data.

transition between faceted and rough interface crystal growth, which is sensitive to alloying.<sup>22–26</sup> While the microstructural development of Bi-Sn alloys has been well studied using traditional metallographic and decanting techniques, rapid faceted growth of solid bismuth from the retained liquid meniscus layer on preexisting surfaces during decanting results in uncertainties surrounding faceted bismuth crystal growth rates and ledge morphologies.<sup>23,26</sup> Real-time imaging provides an opportunity to dynamically study bismuth crystal growth morphologies and kinetics in Bi-Sn alloys over multiple length scales to improve our understanding of microstructural development.

Figure 1 shows multiscale solidification structures in Bi-Sn alloys. A representative x-ray image, highlighting faceted primary bismuth crystal growth in a 0.1-mm-thick Bi-Sn alloy section, is shown in Fig. 1a. Clearly, the spatial resolution

afforded by x-ray imaging provides microscopic structural information for this constrained thickness across an imaging field of view on the order of several square millimeters. Representative proton images from thin and thick sections are shown in Fig. 1b–e. Proton imaging allows for the dynamic visualization of bismuth crystals and the measurement of crystal sizes and size distributions during growth. Solid–liquid interface macrosegregation is also visible in Fig. 1d. Growth rates of individual crystals would be difficult to assess by traditional metallographic examinations, and liquid metal decanting would preclude measurements of solute segregation in the liquid. Proton imaging can also be used to assess casting design. A single image from a 20-Hz video of a Sn-30 at.% Bi alloy casting mold filling is shown in Fig. 1e. Direct imaging of casting permits the visualization of metal fluid flow and reveals dynamic melt/mold interactions.



Figure 2a further highlights the growth of a crystal ledge on a faceted bismuth crystal in a 0.1-mm-thick Bi-30 at.% Sn alloy during directional solidification in a constant gradient of  $10^{\circ}\text{C cm}^{-1}$  at a cooling rate of  $20^{\circ}\text{C min}^{-1}$ . Absorption of the x-rays creates the primary contrast in the image in Fig. 2a; the highly absorptive primary bismuth crystal therefore appears dark compared with the adjacent tin-rich liquid. Figure 2b summarizes the velocity and height of the ledge seen in Fig. 2a as a function of time starting 35 s after the crystal's first

appearance in the x-ray images. At the time of the first ledge height measurement, the bismuth crystal is approximately  $280\text{ }\mu\text{m}$  across, which is almost three times the foil thickness. The crystal is likely continuous between the crucibles walls at this point, and the growing faces are assumed to be perpendicular to the imaging direction. The initial ledge velocity was rapid, around  $3\text{ }\mu\text{m s}^{-1}$ , but it quickly decreased to zero after 60 s of growth. Correspondingly, the height of the ledge initially increased to approximately  $22\text{ }\mu\text{m}$  before decreasing with increasing time up to about 60 s, ending with a stable ledge height of  $13\text{ }\mu\text{m}$ .

Using the ledge height and velocity data from Fig. 2b, the volumetric growth rate of the ledge was calculated; these data are shown in Fig. 3. The volumetric ledge growth rate decreased monotonically from an initial value of approximately  $0.36\text{ mm}^3\text{ min}^{-1}$  to nearly zero. The overall volumetric growth rate of the crystal is also shown in Fig. 3, calculated by measuring the total area of the crystal, assuming a 0.1-mm thickness. The overall growth rate of the crystal decreased with increasing time, starting at approximately  $23\text{ mm}^3\text{ min}^{-1}$  before the nucleation of the ledge and decreasing to approximately  $5\text{ mm}^3\text{ min}^{-1}$ . After the initiation of the ledge in Fig. 2b, the overall growth rate of the crystal remained relatively constant, within the experimental scatter in the data, at about  $2\text{ mm}^3\text{ min}^{-1}$ . The relatively low volumetric growth rate of the ledge compared with the overall crystal suggests pseudo-ledge growth, rather than true ledge growth, for this example.<sup>27</sup>

The thin foil shown in Fig. 2a was also imaged using the  $\times 7$  magnifier at pRad, as shown in Fig. 4, representing the first demonstration of structural imaging of a metal at  $\sim 25\text{ }\mu\text{m}$  spatial resolution using protons. In the proton image, the multiple scattering of protons by denser features in the

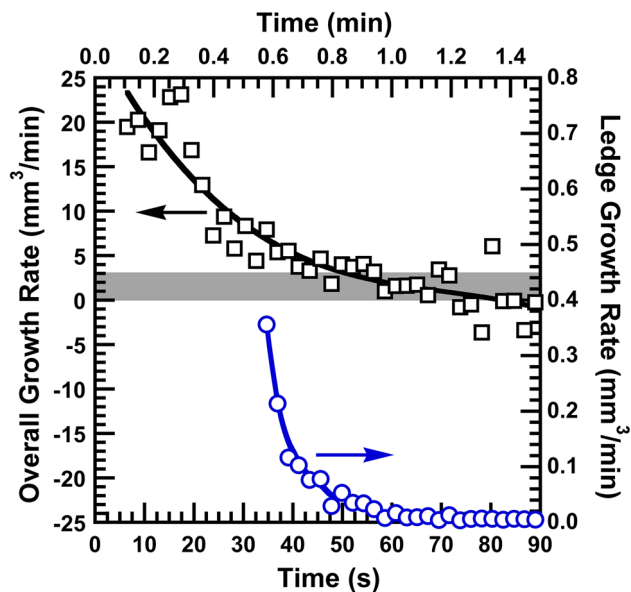


Fig. 3. Overall (left axis, squares) and ledge (right axis, circles) volumetric growth rates for the isolated primary bismuth crystal in Fig. 2a as a function of time. Times are indexed to the first frame showing the growth of the crystal. The shaded band corresponds to growth rates measured during directional solidification of a 0.5-mm-thick section imaged with the  $\times 7$  magnifier at pRad. The lines are intended as a visual guide of the data.

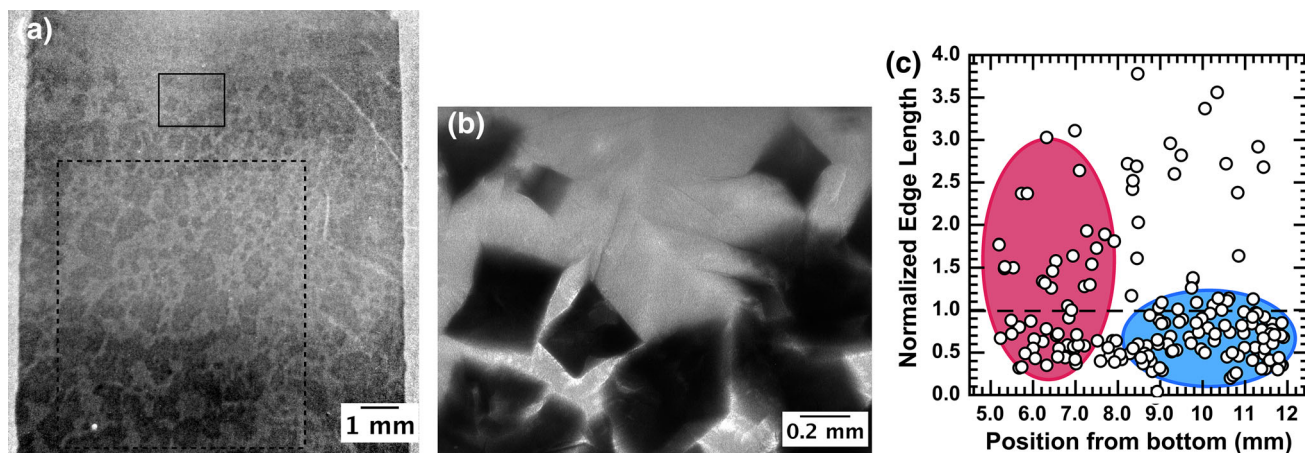


Fig. 4. Direct comparison between (a) a static pRad and (b) an x-ray images from a dynamic sequence of the same 0.1-mm-thick Bi-30 at.% Sn alloy foil. (c) Measured bismuth crystal size as a function of distance from the bottom of the foil in Fig. 4a. The plotted effective edge lengths are normalized to the mean effective edge length ( $260\text{ }\mu\text{m}$ ), assuming a square projected cross section. The solid box indicated in (a) corresponds to the imaged region in (b), whereas the dashed box in (a) highlights the region used to make the measurements in (c).

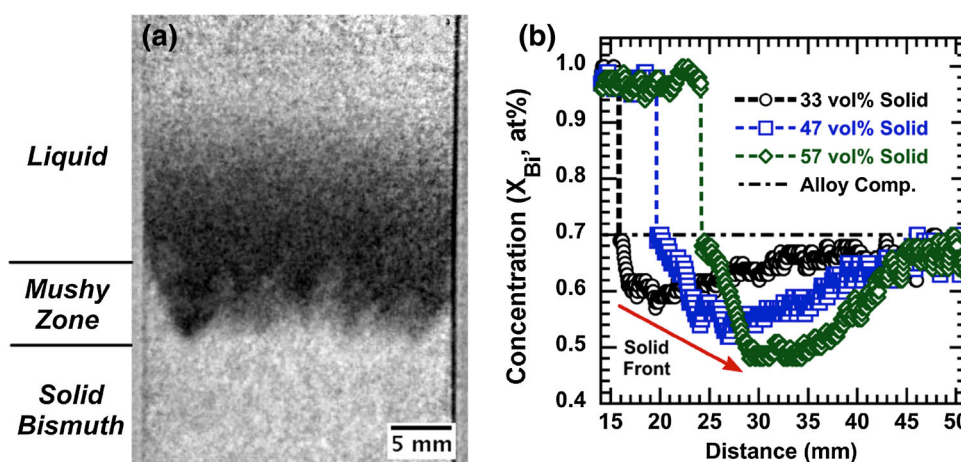


Fig. 5. (a) Areal density map from a proton radiograph of directional solidification of a 6.5-mm-thick, Bi-30 at.% Sn alloy solidified in a constant gradient of  $5^{\circ}\text{C cm}^{-1}$  at a cooling rate of  $2^{\circ}\text{C min}^{-1}$  showing the effect of solute pile-up on density variation in the liquid near the solid-liquid interface. Dark regions in the image correspond to lower density. (b) Concentration changes across the interface as a function of distance from the bottom of the sample for three progressive increments of primary bismuth solid fraction, as measured from proton radiographs.

sample creates darker regions in the image; bismuth-rich regions therefore appear darker than the tin-rich regions. Detailed features of the bismuth crystals, such as ledges, are not resolvable in the pRad image in Fig. 4a, but the larger field of view permits the measurement of bismuth crystal sizes and distribution. Figure 4c shows the relative crystal sizes of 179 individual crystals measured from a reduced area in Fig. 4a (shown by the dashed box in Fig. 4a); the crystal sizes in Fig. 4c are normalized to the average effective edge length of  $260\text{ }\mu\text{m}$ , assuming a square projected cross-section, and they are plotted as a function of vertical position within the sample. Several larger crystals are visible in the measured region in Fig. 4a, which may represent overlapping, or adjacent, individual crystals. These large clusters were treated as a single large particle for the crystal size measurements because they likely would have interacted during growth and the individual crystals could not be separated in the images. Qualitatively, there seems to be a higher density of smaller crystals at the top of the section, near where the x-ray image measurements associated with Figs. 2 and 3 were made. The gradient in bismuth crystal size implies that the local conditions for growth varied along the length of the foil. There were minimal changes in crystal size in the horizontal direction at either the top or the bottom of the measured region in Fig. 4a. The relatively flat thermal gradient imposed on the sample during directional solidification likely minimized horizontal nucleation and growth rate changes in the sample, whereas solute segregation resulting from directional solidification likely enhanced the crystal size variations in the vertical direction.

Proton imaging with the  $\times 7$  magnifier also enabled dynamic imaging of high-density alloy

solidification in thicker sections than those achievable with x-rays. The image in Fig. 1c is a frame from a proton video of directional solidification of a 0.5-mm-thick Bi-30 at.% Sn alloy section in a constant thermal gradient of  $65^{\circ}\text{C cm}^{-1}$  and a cooling rate of  $40^{\circ}\text{C min}^{-1}$ . Projection through a thick cross section (0.5 mm compared with the 0.1-mm-thick x-ray foil) and overlapping crystals makes interpretation of the images more difficult, particularly with respect to volume fraction determinations. The initial growth rate of individual crystals can be readily quantified, however. The overall volumetric bismuth crystal growth rate after the first appearance of bismuth crystals within the top 3 mm of the section was approximately  $2.31 \pm 0.75\text{ mm}^3\text{ min}^{-1}$ , whereas the growth rate within the lower 5 mm of the section was  $1.39 \pm 1.0\text{ mm}^3\text{ min}^{-1}$ . The growth rates measured during directional solidification of the 0.5-mm-thick section are indicated in the shaded band in Fig. 3. The growth rate of individual crystals in the “thick” section are consistent with those measured for the individual bismuth crystal in the x-ray images prior to the decrease in individual crystal growth rate during final solidification. While the x-ray images represent the growth of a single crystal in a relatively constrained volume of liquid (the crystal edge length exceeds the foil thickness 6 s after the initiation of growth), the good agreement between the overall growth rates measured in the thick and thin sections emphasizes that, in cases where local transport criteria are prevalent compared with long-range parameters, thin sample measurements can be used to accurately inform larger length scale understanding.

Proton radiography also enables imaging of large fields of view and thick sections with the  $\times 3$  magnifier and identity lenses (approximately  $44 \times 44\text{ mm}$  and  $120 \times 120\text{ mm}$ , respectively).

Figure 5a shows a representative proton density map during directional solidification of a 6.5-mm-thick section ( $25 \times 50$  mm width and height) of a Bi-30 at.% Sn alloy solidified in a constant gradient of  $5^\circ\text{C cm}^{-1}$  at a cooling rate of  $2^\circ\text{C min}^{-1}$ . In Fig. 5a, light regions correspond to high areal density, whereas dark regions represent lower density; this is inverse contrast compared with the image shown in Fig. 1d. The entire sample height is not visible in Fig. 5a; the bottom of the image is approximately 14 mm up from the bottom of the section. Individual bismuth crystals cannot be easily resolved in this image, although some crystals are visible in front of the solid–liquid interface. A clear contrast change is observed along the length of the sample in Fig. 5a, particularly near the solid–liquid interface. The contrast variation corresponds to projected density changes from the primary bismuth crystals at the bottom of the sample up through the tin-rich solutal gradient within the liquid near the solid–liquid interface. Figure 5b shows the measured local concentration of bismuth along the section length within the field of view for increasing increments of solid fraction and time. To calculate concentration from the contrast variations in Fig. 5a, the areal density of the sample was first calculated using the known constant density of the graphite crucible adjacent to the sample, which was then correlated with the observed density contrast. The density variation within the liquid was then converted to concentration using Eq. 1.

$$X_{\text{Bi}} = 0.27\rho_s - 1.87 \quad (1)$$

where  $\rho_s$  is the calculated density of the sample from the proton radiograph and  $X_{\text{Bi}}$  is the concentration of bismuth in the liquid. Equation 1 was determined by linear regression to known liquid densities for several Bi–Sn alloys from the literature, as well as the densities of the pure elements.<sup>28–31</sup> Equation 1 does not describe the density of the solid primary bismuth at the bottom of the sample. The density of first solid at the bottom of the sample was consistent with the expected density of bismuth,  $9.4 \pm 0.1 \text{ kg m}^{-3}$ ; the plateau in density at smaller distances from the bottom of the section in Fig. 5b were forced to fit a concentration representing pure bismuth. In front of the solid bismuth layer, each of the concentration profiles exhibit a region of initially decreasing bismuth concentration with increasing distance. This region corresponds to the two-phase solid/liquid mushy zone. The tin concentration in the mushy zone may not be accurately represented because the presence of solid bismuth was not included in Eq. 1. Beyond the mushy zone, the bismuth concentration increases with increasing distance, and the long-range concentration of bismuth in the liquid eventually approaches the bulk alloy composition.

The rejection of tin during the growth of the primary bismuth crystals resulted in a zone of lower

density liquid in front of the solid–liquid interface. The results in Fig. 5b provide a quantitative measure of the development of macrosegregation during directional solidification. The concentration profiles in Fig. 5b show that the solute boundary layer extends several millimeters in front of the mushy zone. Using the ratio of the tin diffusivity in the alloy liquid ( $1.0 \text{ e}^{-8} \text{ m s}^{-1}$ ) and an approximate growth velocity for the primary bismuth at the bottom of the section (approximately  $40 \mu\text{m s}^{-1}$ ), a boundary layer thickness of approximately 0.2 mm is estimated. Even the relatively slow solidification of this  $25 \times 50 \times 6.5$ -mm sample results in a substantially thicker diffusive layer than predicted, assuming purely diffusive mixing.<sup>23,26,32</sup> The solute-enriched layer also emphasizes that a complete mixing assumption is not valid in this case, while complex transport mechanisms likely provide more rapid mixing than diffusion alone.

The long-range boundary layer of tin in the liquid may also lend some insight into the relative growth rates observed for the bismuth crystals in Figs. 2b and 1c. In both cases, bismuth crystals nucleate in advance of the overall solidification interface in a region that has relatively high tin concentration (see Fig. 5b). With increasing solid fraction in the section, the local solute environment adjacent to the isolated crystals is further increased in tin. Initial growth in a highly supersaturated environment likely dictated the initial rapid growth rate seen in Fig. 3, whereas the subsequent decrease in local supersaturation in the liquid adjacent to the growing crystal resulted in the precipitous decrease in growth rate.

In addition to obtaining growth rates in a solute field, the observation of sedimentation during directional solidification informs the interpretation of local phase fractions. The volume fraction of bismuth crystals in the 100- $\mu\text{m}$ -thick section shown in Fig. 4a was quantified using point counting; the measured primary bismuth volume fraction was  $60 \pm 0.4 \text{ vol.}\%$ . The volume fraction of primary bismuth was also estimated from the proton image of the 6.5-mm-thick section in Fig. 1d; the measured volume fraction of primary bismuth was  $57 \pm 0.2 \text{ vol.}\%$ . While rigorous measurements of the as-solidified 6.5-mm-thick sample from Fig. 5a were not made, metallographic observations of the section suggest that the primary bismuth crystals constitute approximately 60% of the total sample volume. These three values agree reasonably well with simple predictions of primary and eutectic constituent volume fractions using the Schiel and equilibrium models that predict a volume fraction of about 55 vol.% primary bismuth.<sup>33</sup> The spatial distribution of bismuth crystals in Fig. 4c and the long-range sedimentation of primary bismuth crystals in Fig. 5a indicate that macrosegregation of bismuth to the bottom of the sample due to primary bismuth crystal growth was substantial, which may explain



the slight discrepancy between the measured and expected amount of bismuth within the field of view.

## CONCLUSION

Multiscale solidification images have been presented that highlight dynamic structural development during solidification. X-rays permit high spatio-temporal resolution imaging of thin metal sections, whereas 800 MeV protons permit imaging of mesoscale and macroscale structural and solutal development in thin and thick metal sections. Proton imaging is also ideally suited to understand casting design and mold filling, including alloy melt fluid flow and macrosegregation. Although bismuth-tin alloys have been presented in this study, the techniques employed to dynamically image metals can also be used to investigate high-density alloys for structural and energy-critical applications, as well as advanced manufacturing. Direct imaging of metal solidification enables unprecedented access to the inherently multiscale nature of solidification processing to enable the identification of critical parameters that must be understood and incorporated into theory and models to achieve predictive capability and the manufacture of materials with improved properties, performance, and reliability.

## ACKNOWLEDGEMENTS

We thank B.J. Hollander, A. Saunders, C.J. Espinoza, C. Danly, the pRad Team, T.V. Beard, R.W. Hudson, B.S. Folks, D.A. Aragon, T.J. Tucker, J.C. Cooley, and K.D. Clarke (LANL) and A. Deriy (ANL-APS) for providing experimental support. This work was supported by the U.S. Department of Energy (DOE), Office of Science, Basic Energy Sciences (BES) Division of Materials Sciences and Engineering under A.J. Clarke's Early Career Award. Use of the APS, an Office of Science User Facility operated for the U.S. DOE Office of Science by Argonne National Laboratory, was supported by the U.S. DOE under contract no. DE-AC02-06CH11357; x-ray data were collected at the Sector 32-ID-C beamline. We also acknowledge Los Alamos National Security, LLC, operator of the Los Alamos National Laboratory under contract number DE-AC52-06NA25396. This work also benefited from the use of the Proton Radiography Facility, a user facility at the Los Alamos Neutron Science Center at Los Alamos National Laboratory, sponsored primarily by NNSA Science Campaigns.

## REFERENCES

- Executive Office of the President of the United States, National Science and Technology Council, *Materials Genome Initiative for Global Competitiveness*, 2011, [http://www.whitehouse.gov/sites/default/files/microsites/ostp/materials\\_genome\\_initiative-final.pdf](http://www.whitehouse.gov/sites/default/files/microsites/ostp/materials_genome_initiative-final.pdf). Accessed 10 July 2014.
- U.S. Department of Energy, *From Quanta to the Continuum: Opportunities for Mesoscale Science, A Report for the Basic Energy Sciences Advisory Committee Mesoscale Science Subcommittee*, 2012, [http://science.energy.gov/~media/bes/pdf/reports/files/OFMS\\_rpt.pdf](http://science.energy.gov/~media/bes/pdf/reports/files/OFMS_rpt.pdf). Accessed 10 July 2014.
- G.W. Crabtree and J.L. Sarrao, *MRS Bull.* 37, 1079 (2012).
- R.H. Mathiesen and L. Arnberg, *Acta Mater.* 53, 947 (2005).
- R.H. Mathiesen and L. Arnberg, *Mater. Sci. Eng. A* 413–414, 283 (2005).
- R.H. Mathiesen, L. Arnberg, H. Nguyen-Thi, and B. Billia, *JOM* 64, 76 (2012).
- G. Reinhart, N. Mangelinck-Noël, H. Nguyen-Thi, T. Schenk, J. Gastaldi, B. Billia, P. Pino, J. Härtwig, and J. Baruchel, *Mater. Sci. Eng. A* 413–413, 384 (2005).
- N. Limodin, L. Salvo, E. Boller, M. Suéry, M. Felberbaum, S. Gailliegue, and K. Madi, *Acta Mater.* 57, 2300 (2009).
- A. Bogno, H. Nguyen-Thi, G. Reinhart, B. Billia, and J. Baruchel, *Acta Mater.* 61, 1303 (2013).
- C. Puncreobutr, P.D. Lee, R.W. Hamilton, and A.B. Phillion, *JOM* 64, 89 (2012).
- A.J. Clarke, S.D. Imhoff, J.C. Cooley, B.M. Patterson, W.-K. Lee, K. Fezzaa, A. Deriy, T.J. Tucker, M.R. Katz, P.J. Gibbs, K.D. Clarke, R.D. Field, D.J. Thoma, and D.F. Teter, *Emerg. Mater. Res.* 2, 1 (2013).
- A. Clarke, S. Imhoff, P. Gibbs, J. Cooley, C. Morris, F. Merrill, B. Hollander, F. Mariam, T. Ott, M. Barker, T. Tucker, W.-K. Lee, K. Fezzaa, A. Deriy, B. Patterson, K. Clarke, J. Montalvo, R. Field, D. Thoma, J. Smith, and D. Teter, *Sci. Rep.* 3, 2020 (2013).
- N.S.P. King, E. Ables, K. Adams, K.R. Alrick, J.F. Amann, S. Balzar, P.D. Barnes Jr, M.L. Crow, S.B. Cushing, J.C. Eddleman, T.T. Fife, P. Flores, D. Fujino, R.A. Gallegos, N.T. Gray, E.P. Hartouni, G.E. Hogan, V.H. Holmes, S.A. Jaramillo, J.N. Knudsson, R.K. London, R.R. Lopez, T.E. McDonald, J.B. McClelland, F.E. Merrill, K.B. Morley, C.L. Morris, F.J. Naivar, E.L. Parker, H.S. Park, P.D. Pazuchanics, C. Pillai, C.M. Riedel, J.S. Sarracino, F.E. Shelley Jr, H.L. Stacy, B.E. Takala, R. Thompson, H.E. Tucker, G.J. Yates, H.-J. Ziock, and J.D. Zumbro, *Nucl. Instrum. Methods A* 424, 84 (1999).
- C.L. Morris, N.S.P. King, K. Kwiatkowski, F.G. Mariam, F.E. Merrill, and A. Saunders, *Rep. Prog. Phys.* 76, 26 (2013).
- P.A. Rigg, C.L. Schwartz, R.S. Hixson, G.E. Hogan, K.K. Kwiatkowski, F.G. Mariam, M. Marr-Lyon, F.E. Merrill, C.L. Morris, P. Rightly, A. Saunders, and D. Tupa, *Phys. Rev. B* 77, 220101 (2008).
- C.T. Mottershead and J.D. Zumbro, *Proc. 1997 Part. Accel. Conf.*, ed. M. Comyn, M.K. Craddock, M. Reiser, and J. Thompson (IEEE, Piscataway, NJ, 1997), pp. 1397–1399.
- T. Mottershead, D. Barlow, B. Blind, G. Hogan, A. Jason, F. Merrill, K. Morley, C. Morris, A. Saunders, and R. Valdiviez, *Proc. 2003 Part. Accel. Conf.*, ed. J. Chew (IEEE, Piscataway, NJ, 2003), pp. 702–704.
- R. Valdiviez, F. Sigler, D. Barlow, B. Blind, A. Jason, T. Mottershead, J. Gomez, and C. Espinoza, *Proc. 2003 Part. Accel. Conf.*, ed. J. Chew (IEEE, Piscataway, NJ, 2003), pp. 1664–1666.
- F.E. Merrill, E. Campos, C. Espinoza, G. Hogan, B. Hollander, J. Lopwz, F.G. Mariam, D. Morley, C.L. Morris, M. Murray, A. Saunders, C. Schwartz, and T.N. Thompson, *Rev. Sci. Instrum.* 82, 1 (2011).
- J. Schindelin, I. Arganda-Carreras, E. Frise, V. Kaynig, M. Longair, T. Pietzsch, S. Preibisch, C. Rueden, S. Saalfeld, B. Schmid, J.-Y. Tinevez, D.J. White, V. Hartenstein, K. Eliceiri, P. Tomancak, and A. Cardona, *Nat. Methods* 9, 331 (2012).
- L.E. Felton, C.H. Raeder, and D.B. Knorr, *JOM* 45, 28 (1993).
- K.A. Jackson, *Growth and Perfection of Crystals*, ed. R.H. Doremus, B.W. Roberts, and D. Turnbull (New York: Wiley, 1958), pp. 319–324.
- K.A. Jackson, D.R. Uhlmann, and J.D. Hunt, *J. Cryst. Growth* 1, 1 (1967).
- H.W. Kerr and W.C. Winegard, *Crystal Growth*, ed. H.S. Peiser (Oxford: Pergamon, 1967), p. 179.

25. M.R. Taylor, R.S. Fidler, and R.W. Smith, *J. Cryst. Growth* 3–4, 666 (1968).
26. M.V. Hecht and H.W. Kerr, *J. Cryst. Growth* 7, 136 (1970).
27. J.W. Cahn, W.B. Hillig, and G.W. Sears, *Acta Metall.* 12, 1421 (1964).
28. J.A. Cahill and A.D. Kirshenbaum, *J. Inorg. Nucl. Chem.* 25, 501 (1963).
29. R.A. Khairulin, S.V. Stankus, R.N. Abdullaev, and V.M. Sklyarchuk, *High Temp.* 48, 206 (2010).
30. M.J. Assael, A.E. Kalyva, K.D. Antoniadis, R.M. Banish, I. Egry, J. Wu, E. Kaschnitz, and W.A. Wakeham, *J. Phys. Chem. Ref. Data* 39, 033105 (2010).
31. Y. Plevachuk, V. Sklyarchuk, G. Gerbeth, S. Eckert, and R. Novakovic, *Surf. Sci.* 605, 1034 (2011).
32. W.A. Tiller, K.A. Jackson, J.W. Rutter, and B. Chalmers, *Acta Metall.* 1, 428 (1953).
33. H. Okamoto, *ASM Alloy Phase Diagrams Center* (Materials Park, OH: ASM International, 1990).